Real-time Wells turbine simulation on an oscillating-water-column wave energy converter physical model

Beatrice Fenu [a],[*], João C.C. Henriques [b], Mattia Glorioso [a], Luís M.C. Gato [b], Mauro Bonfanti [a]

[a] *Politecnico di Torino, Department of Aerospace and Mechanical Engineering, Corso Duca degli Abruzzi, 24, Torino, 10124, Italy*
[b] *LAETA, IDMEC, Instituto Superior Técnico, Universidade de Lisboa, Av. Rovisco Pais, 1049-001, Lisbon, Portugal*

ARTICLE INFO

ABSTRACT

Due to its simplicity and low cost, the Wells turbine is the most common choice for driving oscillating-water-column (OWC) wave energy converters (WECs) power take-off system. This turbine is characterized by a flow rate that is a linear function of the pressure head and inversely proportional to the rotational speed before the onset of hard stall conditions. The Wells turbine has been simulated in wave tanks using porous plugs, where the flow rate exhibits linear behaviour. However, numerical and experimental results have shown that rotational speed variations significantly influence the performance of OWC WECs. This work aims to develop a novel real-time simulator of a Wells turbine for use in physical models of OWC power plants. The proposed simulator consists of a diaphragm whose diameter is adjusted in real-time as a function of the pressure head measured in the laboratory and the rotational speed calculated by a hardware-in-the-loop model. In this way, it is possible to reproduce the full behaviour of the Wells turbine before and after a hard stall. Experimental results demonstrate the effectiveness of the simulator. A performance analysis was conducted to understand the device's potential and compare the damping that Wells and impulse turbines introduce.

1. Introduction

Renewable energy sources are pivotal in the shift towards energy systems that are less carbon-intensive and more sustainable. Recent years have seen a rapid expansion in installed capacity of solar and wind energy driven by policy initiatives and significant cost reductions. Among the renewable energy sources, wave energy remains the world's largest unexploited source. According to the Intergovernmental Panel on Climate Change (IPCC) [1], the global annual wave energy production potential is estimated at 29,500 TWh/year, almost ten times Europe's electricity demand [2]. For this reason, the harnessing and conversion of wave energy has driven the exploration of new technologies to pursue the necessity of producing electrical energy from renewable resources.

Various wave energy converter (WEC) technologies have undergone development and examination through numerical simulations and experimental analysis [3]. Examples of advances in existing technologies are detailed in recent reviews [4,5]. Among the WEC devices already investigated, oscillating water columns (OWCs) are particularly advantageous due to their simple design, with all moving mechanical parts located outside of the water. The OWC technology has been developed for a wide range of water depths, making it a versatile option for wave energy conversion [6]. This type of system uses the movement of the water surface inside an air chamber to create bidirectional airflow. The pneumatic energy is converted into electrical energy by an air turbine connected to an electrical generator via a shaft, which forms the system's power take-off (PTO).

OWC devices have been extensively studied and a wide variety of configurations have been developed with the goal of maximizing their efficiency and reducing costs [7]. Floating OWCs deployed in the deep sea are considered the best option for large-scale energy exploitation [8–13], and the integration of OWCs in floating wind turbines represents an advance in floating technology to reduce the levelized cost of energy (LCoE) [14].

Another way to reduce the LCoE is to integrate multiple OWC power plants into breakwaters when they are built [15]. The Mutriku power plant is the most noteworthy example of this approach [16]. This grid-connected plant has been in continuous operation since 2011. In 2003, Boccotti proposed a new fixed OWC configuration – called the U-OWC – in which the submerged part of the OWC opens upwards instead of horizontally [17]. This design allows a longer OWC and therefore a lower resonant frequency, without the drawback of having a deeply submerged opening. Following the success of the Mutriku wave power plant, the first fully operational U-shaped OWC facility
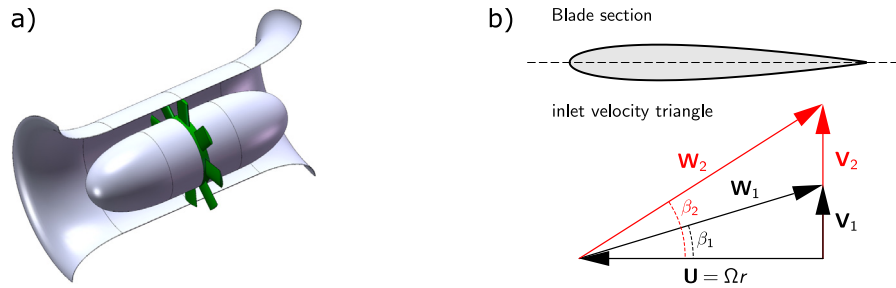
Fig. 1. (a) A Wells turbine without guide vanes. (b) A typical aerofoil section of a rotor blade and the inlet velocity triangles for two flow rates [22].

was successfully installed in Civitavecchia, Italy [17]. This plant consists of resonant wave energy converter (REWEC3) caissons, with the monitoring conducted by Arena et al. [18] focusing on a single chamber of the full-scale plant and the validation of the numerical model with small-scale experiments [19].

Of the various ways of converting pneumatic energy into mechanical energy from an OWC, Wells turbines and impulse turbines are the most widely studied. In this paper, the focus is on Wells turbines, but impulse turbines are also included to fully understand the discussion, as they are used as a benchmark to compare the performance of the device. Wells turbines, shown in Fig. 1, are the most commonly used to equip OWC plants due to their simplicity and low cost. However, this type of turbine is characterised by a narrow operating range with high efficiency [20]. Alternatively, axial impulse turbines have also been studied and tested in OWC devices [21]. While these turbines lack the hard stall behaviour of Wells turbines, they suffer from the disadvantage of significant losses in the exit guide vanes.

Experimental testing is critical to evaluating the performance of WECs, providing valuable data on their efficiency and effectiveness. In addition, experimental results can help optimize the design of WECs to improve their performance, for example by controlling platform movements to improve energy capture. Furthermore, experimental testing allows the assessment of laboratory effects and the consistency of results, which is essential to ensure the reliability and reproducibility of WEC performance assessments [23].

In OWC model testing, air turbines cannot be accurately simulated if the Reynolds number based on tip speed and rotor radius is much less than 10^6. This is the case for OWC model testing in wave tanks or wave flumes, where turbines are replaced by simulators. The type of turbine simulator depends on whether the turbine is of the Wells or the impulse type. Wells turbines show an approximately linear relationship between the flow rate coefficient and the pressure coefficient. It can be shown that the flow Q is related to the pressure drop Δp across the Wells turbine by $Q \propto \Delta p / \Omega$, where Ω is the rotational speed of the turbine.

The standard procedure for simulating a Wells turbine in a wave tank model has been to assume a constant rotational speed and find a laminar flow device with a linear pressure drop suitable for modelling a small-scale turbine. The typical Wells turbine simulator consists of layers of textile materials. These simulators have a linear pressure-flow relationship when designed to maintain laminar flow through their material [24,25]. These approaches require particular care in their implementation, as the textile/porous material placed in a humid environment may be subject to water absorption. In addition, the variations in turbine rotational speed are always neglected. On the other hand, impulse turbines have an approximately quadratic relationship between the flow coefficient and the pressure coefficient such that $Q \propto \sqrt{\Delta p}$, which is independent of the rotational speed. This type of relationship is similar to that of turbulent flow through an orifice plate.

From the recent literature, several studies on OWC demonstrate the effect of PTO size through experimental analysis. Among the most recent investigations, Cheng et al. [26,27] present different PTO configurations as fixed area orifices and aerodynamic dampers and their

effect on the hydrodynamics of the system, finding that PTO damping plays a dominant role in both the overall conversion efficiency and the transmission coefficient. Additional analysis on the impulse air turbine has been carried out experimentally by Liu et al. [28] and Joensen et al. [29] with the aim of investigating the operational performance of the WEC devices. In contrast, experimental work on the Wells turbine focuses on the aerodynamic aspect [30].

The purpose of this paper is to implement a new and highly accurate methodology for simulating Wells turbines in small scale wave tank tests. The novelties are:

- include the effects of turbine rotational speed variations;
- provide the ability to simulate a specific turbine geometry in real-time by implementing its dimensionless characteristic curves;
- allow different turbine control strategies to be tested and compared.

A hardware-in-the-loop (HIL) methodology was used for the simulation of the Wells turbine [31]. To this end, the Wells turbine is simulated with a diaphragm whose area is controlled in real-time to reproduce the instantaneous flow rate of the turbine. The turbine rotational speed is calculated by a HIL model using the experimental pressure measured in real-time in the OWC device. This is a new application of the HIL technique to experimentally simulate the complete PTO system of an OWC WEC. The new Wells turbine simulator concept was tested and validated on a fixed U-shaped OWC model. The turbine geometry is the same as that of the Mutriku plant.

The paper is structured as follow: Section 2 describes the model considered to represent the air turbine, focusing on the PTO system model and presenting Wells and impulse turbines. Section 3 presents in detail the experimental program, specifically the description of the facility and the scaled model, the data acquisition system and the implementation of the real-time model together with the scaling procedure. In Section 4 the wave generation is analysed and the hydrodynamic behaviour is presented for the optimal turbine size. Finally, the results and conclusions are reported in Sections 5 and 6, respectively.

2. Power take off dynamics

The study refers to a fixed U-OWC whose side view is shown in Fig. 2. This geometry has been optimized for inclusion in a breakwater structure for a site on the coast of northern of Portugal, see [32] for further details. The U-OWC system dynamics revolve around the interplay among the OWC hydrodynamics, the air chamber thermodynamics, and the PTO subsystem dynamics and control. The numerical modelling of the hydrodynamics of a fixed OWC is beyond of the scope of the current paper. A review of the topic can be found in [7]. The thermodynamic model representing the dynamic behaviour of the air chamber is based on the hypothesis that air behaves as an ideal gas and that compression/expansion is an isentropic process. These hypotheses and the derivation of the equations presented in Section 2 are detailed in [33]. Consequently, the compression and expansion process can be described by

$$\frac{\Delta \dot{p}}{\Delta p + p_{\text{atm}}} = -\gamma \left(\frac{\dot{V}_c}{V_c} + \frac{\dot{m}_{\text{turb}}}{\rho_c V_c} \right), \tag{1}$$
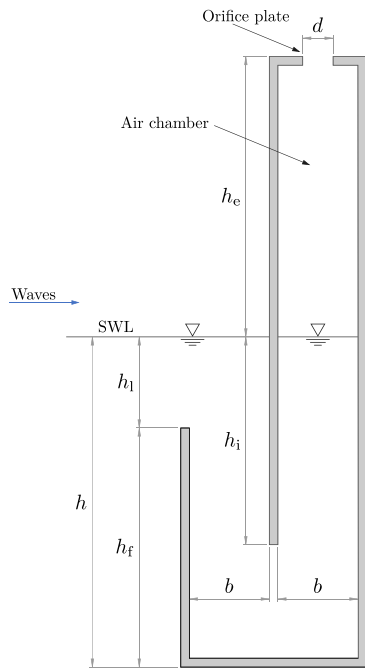
(a) Longitudinal cut.
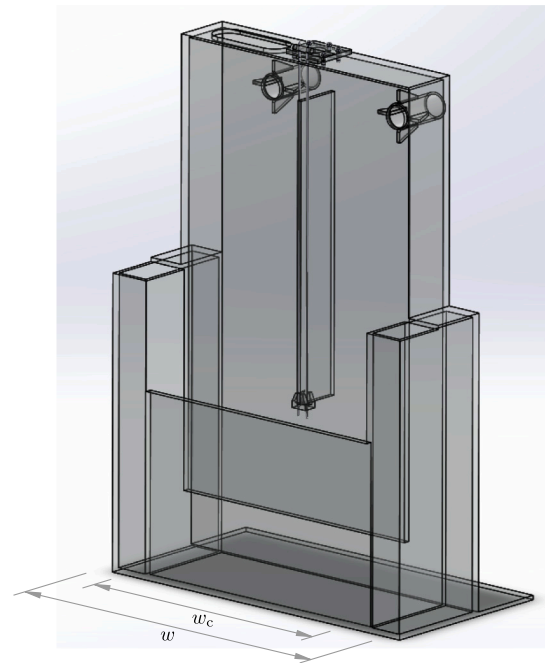
(b) Three-dimensional view.

Fig. 2. The U-OWC power plant model.

where Δp is the pressure variation relative to the atmosphere, p_{atm} is the atmospheric pressure, V_c is the instantaneous volume of the air chamber, $\dot{m}_{turb}$ is the mass flow rate through the turbine, and ρ_c is the air density inside the chamber calculated by the isentropic relationship

$$\rho_c = \rho_{atm} \left(\frac{\Delta p}{p_{atm}} - 1 \right)^{1/\gamma}. \tag{2}$$

The PTO consists of an air turbine that drives an electric generator. The turbine's flow rate and the shaft power are usually computed using the non-dimensional functions

$$\Phi = f_\Phi(\Psi) \tag{3}$$

and

$$\Pi = f_\Pi(\Psi), \tag{4}$$

such that

$$\Psi = \frac{\Delta p}{\rho_{in} \Omega^2 D^2}, \tag{5}$$

$$\Phi = \frac{\dot{m}_{turb}}{\rho_{in} \Omega D^3}, \tag{6}$$

$$\Pi = \frac{P_{turb}}{\rho_{in} \Omega^3 D^5}. \tag{7}$$

Here Φ is the flow coefficient, ρ_{in} is the air density at turbine inlet stagnation conditions, Ω is the rotational speed of the turbine, D is the turbine rotor diameter, P_{turb} the turbine instantaneous power output, and Δp is pressure drop across the turbine. The functions (3) and (4) are valid for large values of the Reynolds number above 10^6 and for low values of the Mach number. The turbine efficiency is defined as the ratio of the extracted power P_{turb} to the available pneumatic power P_{pneu}, as follows

$$\eta_{turb} = \frac{P_{turb}}{P_{pneu}} = \frac{\Pi}{\Phi \Psi}. \tag{8}$$

The dynamics of the PTO system is modelled through

$$I\dot{\Omega} = \frac{P_{turb} - P_{gen}}{\Omega}, \tag{9}$$

where I is the inertia of the rotating components of the PTO system. The power of the turbine can be calculated from

$$P_{turb} = \rho_{in} \Omega^3 D^5 f_\Pi(\Psi). \tag{10}$$

Numerous control laws for OWC generators have been suggested. For the sake of simplicity, but without loss of generality, the following control law has been adopted in the present experimental work

$$P_{gen}^{opt} = a \Omega^b. \tag{11}$$

The parameter b is usually considered equal to 3, see [35] for further details. For the Wells turbine, the parameter a has to be tuned depending on the mean pressure inside the air chamber for different sea states.

To avoid operating the generator above the generator rated power P_{gen}^{rated}, the effective applied power is calculated as

$$P_{gen} = \min\left(P_{gen}^{opt}, P_{gen}^{rated} \right). \tag{12}$$

As reported in [36], the Wells turbine is well represented by a linear relationship between the pressure coefficient and the flow rate coefficient, such that

$$\Psi = c_W \Phi, \tag{13}$$

where c_W is a dimensionless constant that is independent from the turbine size and the rotational speed, and varies depending only on the geometry of the turbine.

The impulse turbine flow coefficient is a non-linear function of the pressure coefficient. To a first approximation, the pressure coefficient is proportional to the square of the flow coefficient [36]

$$\Psi = c_I \Phi^2, \tag{14}$$

where c_I is a dimensionless constant.

Using Eqs. (13) and (14), mass flow rate for both turbines can be expressed as

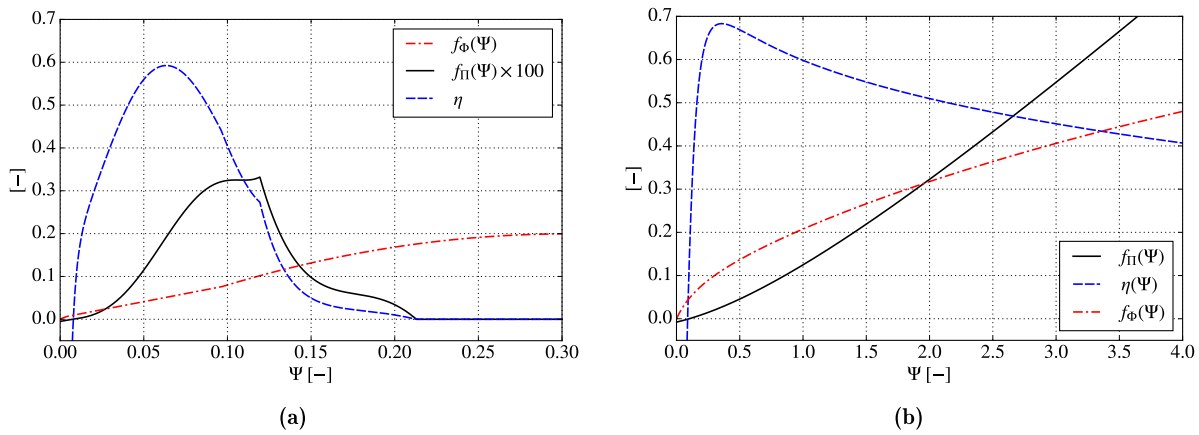$$\dot{m}_W = \frac{D}{c_W} \frac{\Delta p}{\Omega}, \tag{15}$$

Fig. 3. Experimental flow rate coefficient curve, f_Φ, power coefficient curve, $f_\Pi \times 100$, and efficiency curve, η_{turb}, as functions of the pressure coefficient, Ψ, for (**a**) the Wells turbine installed at the Mutriku power plant [34], (**b**) the biraidal (impulse) turbine tested at Mutriku power plant [35].

and

$$\dot{m}_{\text{I}} = \frac{D^2}{\sqrt{c_{\text{I}}}} \sqrt{\rho \Delta p}. \tag{16}$$

In both turbines, the mass flow rate depends on the turbine rotor diameter and the available pressure head. However, in the case of the Wells turbine, it also depends on the rotational speed, which means that the flow rate is affected by the turbine control. Therefore, the hydrodynamic behaviour of the system is indirectly affected by the control, as the pressure force in the air chamber affects the dynamics of the water column. Coupled control of the turbine generator set with the hydrodynamics should be considered for optimum performance, which results in rotational speed variation.

This paper presents an experimental technique to simulate the Wells turbine according to the experimental flow curve

$$Q_{\text{turb}} = \Omega D^3 f_\Phi(\Psi). \tag{17}$$

The aim was to overcome the limitations of simulating the Wells turbine in wave tank tests, namely: (i) the assumption of a constant rotational speed; (ii) the porous material can change its properties when exposed to the humidity of the tank environment. By considering the full flow curve of the Wells turbine, it is also possible to simulate its hard stall behaviour, see Fig. 3. For sake of completeness, Fig. 3 shows also the related curves for an impulse turbine.

3. Experimental program

The aim of the experimental campaign was to simulate a Wells turbine using a diaphragm whose the diameter is adjusted in real-time to set the instantaneous flow rate according to Eq. (17). The results obtained are then used to compare the Wells turbine with a impulse turbine.

3.1. Facility

The experimental program was conducted in the wave flume of Instituto Superior Técnico in Lisbon, Portugal. The wave flume has a length of 20 m, a width of 0.7 m and a depth of 0.5 m. It is equipped with a piston-type wave maker located on one end of the flume. The fixed U-OWC model was installed on the other end. Three resistive wave gauges were placed along the flume to measure the generated waves at different distances between the wave maker and the scaled prototype, namely 6, 9.5 and 16 m from the wave maker. Fig. 4 shows the setup of the wave probes.

3.2. Model description

A longitudinal cut and a three-dimensional view of the model of the fixed U-OWC structure is presented in Fig. 2. The U-OWC power plant and waves were scaled down using Froude similarity. The geometric scaling factor chosen was $\varepsilon = 1/43.5$, based on the maximum length of the prototype allowed by the width of the wave flume.

The model was constructed in acrylic glass to observe the behaviour of the water column inside the scaled model, see Fig. 5 (a) and (b). The water depth of the flume was set to 0.414 m in still conditions. The volume of the air chamber model, V_{m}, was scaled to simulate the spring-like compressibility of the air in the chamber as described in the Ref. [33], thus yielding

$$V_{\text{m}} = \frac{\rho_{\text{p}}}{\rho_{\text{m}}} \varepsilon^2 V_{\text{p}}, \tag{18}$$

where V_{m} is the air chamber volume of the model, ρ_{p} is the water density used in the prototype, ρ_{m} is the density of the water used in the wave flume, and V_{p} is the air chamber volume of the prototype. The scaling process gives an equivalent V_{m} that is significantly larger than the volume of the scaled model. To ensure the correct volume of the air chamber model, two oil barrels were connected to the air chamber by two rigid hoses, see Fig. 5(c). The geometric characteristics of the prototype and the model are described in the Table 1.

The scaled model was equipped with three resistive wave gauges to measure the water level inside the chamber and two Honeywell differential pressure sensors to measure the air chamber pressure relative to the atmosphere. A diaphragm was installed at the top of the air chamber to simulate the air turbine, Fig. 5 (d). The diaphragm was operated by a mechanical arm connected to a servomotor that could open and close it within a diameter range of 0 to 75 mm, with a maximum speed of 0.13 s/60°. The opening and closing speed has been chosen to be appropriate to ensure dynamics that follow the diameter set point as closely as possible. The servomotor was connected by a shaft to an encoder to measure the aperture of the diaphragm. The diaphragm dimensions were chosen based on the highest area ratio in test planning. Furthermore, a diaphragm capable of fully closing in accordance with the dynamic expectations of the numerically simulated system was selected.

3.3. Data acquisition system and real-time model implementation

The data acquisition system was developed in Labview software and a myRIO 1900 board was used to manage the experiment. The experiment comprised three parts: the physical model, the hardware in the loop simulator and the time domain model of the PTO system, as shown in Fig. 6.
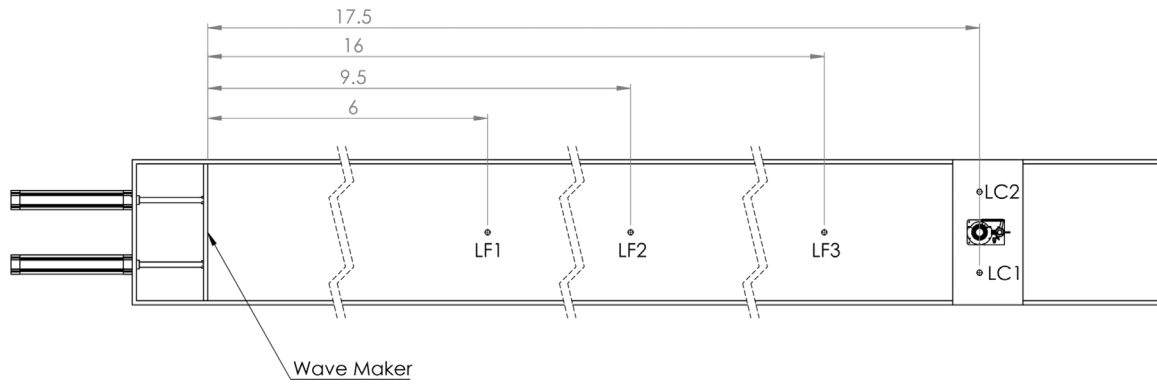
Fig. 4. Top view of wave tank scheme setup, showing the location of wave maker, scaled model and three wave probes respectively named LF1, LF2, LF3, at the distance from the wavemaker of 6, 9.5 and 16 m.
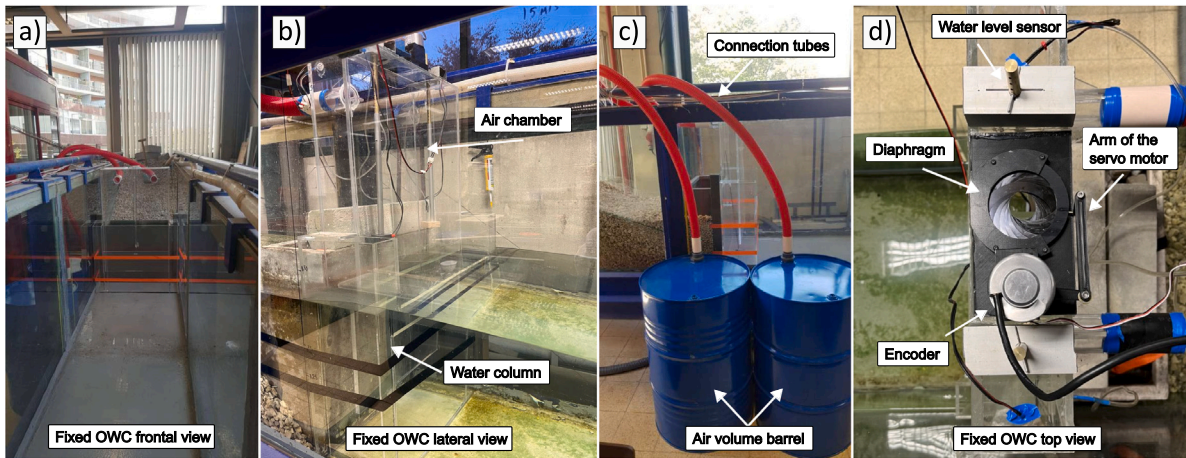

Fig. 5. (a) Front and (b) side views of the model. (c) View of the oil barrels that were attached to the air chamber to ensure the scaling of the spring-like air compressibility effects. (d) Top view of the model scale showing the diaphragm.

Table 1
Full scale and scaled parameters of fixed OWC.

Name	Symbol	Full scale [m]	Scaled model [m]
Air chamber height	h_e	12	0.276
Air chamber width	w_c	23	0.530
Front wall height	h_f	15	0.345
Internal height	h_i	12	0.276
Internal length	b	4	0.092
Lip height	h_l	12	0.276
Orifice diameter	d	1.35	0.031
Power plant width	w	30	0.690
Water depth	h	18	0.414

The physical model refers to the U-OWC power plant, the OWC, the air chamber, the two pressure sensors, the two resistive wave gauges, the diaphragm, the servo motor and the encoder. The myRIO collects the pressure variation Δp of the air chamber and outputs a PWM signal to control the servomotor. In addition, the encoder measures the diameter of the diaphragm D_{fb}, which returns a signal to the myRIO. The HIL simulator runs on Labview 2019, which acquires all the signals and runs the Simulink/Matlab real-time model.

The real-time model uses the measured pressure variation to solve the dynamic equation of the air turbine (Eq. (9)). The Wells turbine was modelled by its dimensionless representation of the performance curves, shown in Fig. 3. The curves were implemented as look-up tables. The PTO control was then applied by using Eq. (12). The turbine flow $\dot{m}_{turb}$ was obtained from the interpolations of the look-up tables. To model the instantaneous flow rate of the Wells turbine, a diaphragm

was installed at the top of the air chamber with real-time control of its aperture. The diaphragm was modelled as an ideal orifice [37] using

$$Q_v = \mathrm{sign}(\Delta p)\, C_D A_d \sqrt{\frac{2|\Delta p|}{\rho_a}}, \tag{19}$$

where C_D is the discharge coefficient assumed to be 0.66, ρ_a is the air density at atmospheric conditions, and A_d is the instantaneous area of the diaphragm. The real-time model calculates the area A_d of the diaphragm from Eq. (19), taking into account the Q_v calculated by the numerical model of the air turbine. Then the diaphragm diameter D_{set} is obtained from A_d, as output. A summary scheme of the implementation of the acquisition system and its logic is presented in Fig. 6.

3.3.1. Scaling procedure

The dynamics of the PTO system are computed in the HIL controller using the turbine, the generator and pressure at prototype scale. Therefore, the time discretization and magnitude of the measured pressure must be scaled up to be an input to the HIL controller. The same reasoning is applied to scale down the output of the HIL controller.

The Froude similarity [38] is used to convert from model to prototype scales and vice versa, giving

$$\frac{t_m}{t_p} = \varepsilon^{1/2}, \tag{20}$$

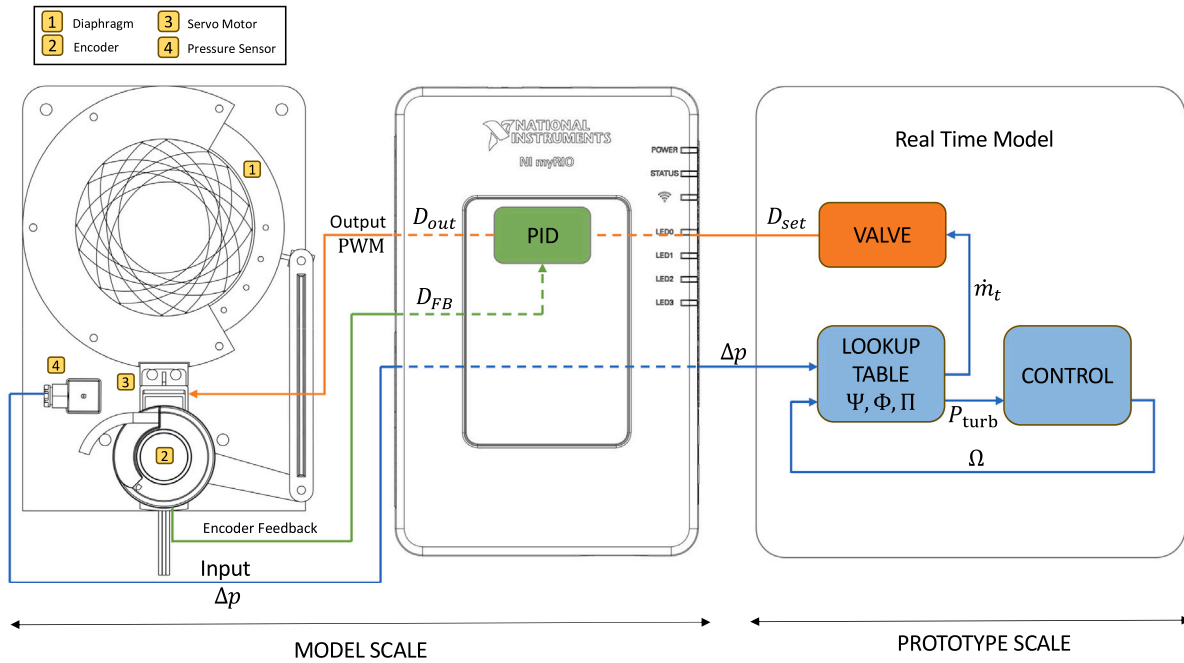$$\frac{\Delta p_m}{\Delta p_p} = \varepsilon, \tag{21}$$

Fig. 6. Setup used during the experiments representing the diaphragm located on top the OWC air chamber, connected with the acquisition system that solves the real-time model of Wells turbine.

Table 2
Summary of diameters and relative area ratio adopted for testing Wells turbine and impulse turbine. S is the ratio between the areas of the air turbine and the OWC chamber.

Wells turbine		Impulse turbine	
Diameter [m]	S [%]	Diameter [m]	S [%]
1.35	1.5	1.02	0.85
1.48	1.8	1.24	1.25
1.56	2.0	1.35	1.5
1.65	2.2	1.65	2.2

where ε is the geometric scaling factor, see Section 3.2. The same scaling procedure can be applied to the turbine flow rate, yielding

$$Q_{\text{turb,m}} = Q_{\text{turb,p}}\, \varepsilon^{5/2}. \tag{22}$$

Using Eq. (22), the turbine flow rate (Eq. (17)) can be related to the flow through the orifice (Eq. (19)) and the instantaneous diaphragm area calculated from Eq. (19).

4. Data analysis

In this Section the wave generation analysis is presented together with the hydrodynamic response of the device and an analysis of the control action on the turbine. Wave flume tests were conducted to demonstrate the Wells turbine simulator's capabilities in various wave conditions, including regular and irregular waves. The Wells turbine is modelled in hardware-in-the-loop and compared to an impulse air turbine represented by a fixed orifice plate. Both cases were studied for different area ratios, calculated as the ratio of the area occupied by the air turbine A_{turb} to the cross-section of the OWC air chamber A_{OWC}, defined as

$$S = \frac{A_{\text{turb}}}{A_{\text{OWC}}}. \tag{23}$$

The area ratios of the Wells turbine are spaced to test different conditions while respecting the mechanical limits as described in Section 4.3 and considering the limit at which variation affects the hydrodynamic response (Section 4.4). All diameters tested are summarized in Table 2.

As far as wave generation is concerned, it is necessary to distinguish between the cases of regular and irregular waves in order to understand what are the limits associated with the wave tank in terms of the accuracy of the generated waves and the reflection effect.

4.1. Regular waves

For regular waves, the analysis was performed selecting a time interval that excludes the effect of the wave reflections caused by front wall of the device. The adequate time interval $t \in [t_1, t_2]$ was defined as

$$t_1 = t_0 + t_{\text{ramp}}, \tag{24}$$

$$t_2 = t_1 + \frac{L_{\text{sr}}}{c_{\text{g}}}, \tag{25}$$

where t_0 is the initial time, t_{ramp} is the ramp time of the wavemaker to generate the wave, L_{sr} is the distance between the wavemaker and the position of the considered sensor, and the group speed c_{g} is obtained from the dispersion relation [39] as

$$c_{\text{g}} = \frac{\omega}{2k}\left(1 + \frac{2kh}{\sinh 2kh}\right), \tag{26}$$

where k is the wave number, h is the water depth, and ω is the angular frequency. Note that the initial waves of the train are transient and propagate on average at the group speed. For a constant water depth equal to $h = 0.414\,\text{m}$, a range of wave frequencies between $0.5\,\text{Hz}$ and $1.1\,\text{Hz}$ is performed. The wave height was kept constant to $H = 0.046\,\text{m}$ for all the frequencies. The range was chosen through a trade off between the wave conditions of interest and the ability of the wave maker to generate proper wave time-series.

4.2. Irregular waves

Irregular waves were generated using a JONSWAP spectral density function (SDF) [40]. It incorporates a scheme of deterministic amplitude with random phases Φ_j, uniformly distributed in the range of $[0, 2\pi]$ [41]. The discretisation of the JONSWAP spectrum S_η generates a wave in $(N + 1)$ frequencies $f = (j + 1)\Delta f$, $j \in 0, \ldots, N$, considering

Table 3
The set of eight sea states used to test the turbine simulator. The sea states were characterized by peak frequency f_p and significant wave height H_s. The experimental data had a standard deviation of σ_{f_p} and σ_{H_s}.

ID	f_p [Hz]	σ_{f_p} [Hz]	H_s [m]	$\sigma_{H_s} \times 10^{-3}$ [m]
s_1	0.94	0.031	0.0238	5.8
s_2	0.77	0.021	0.0174	1.0
s_3	0.75	0.020	0.0226	1.4
s_4	0.67	0.005	0.0219	0.8
s_5	0.74	0.030	0.0332	0.9
s_6	0.50	0.003	0.0404	3.4
s_7	0.60	0.007	0.0346	0.9
s_8	0.52	0.006	0.0266	1.1

Table 4
Characteristics of the reference Wells turbine optimized for the present device under North Atlantic wave energy resource.

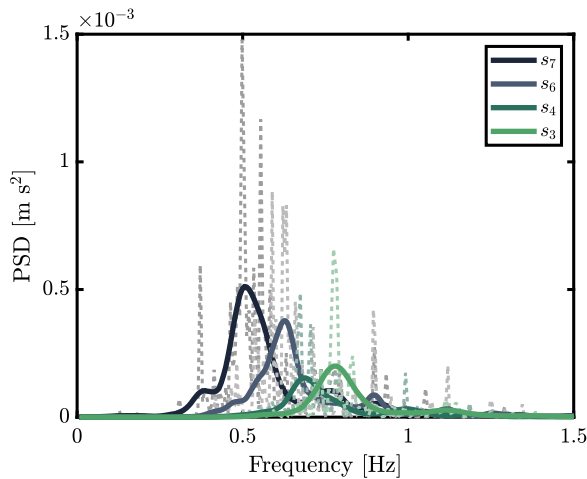| Name	Symbol	Value	Unit
Diameter	D_{ref}	1.35	m
Inertia	I_{ref}	60	$kg\,m^2$
Nominal rotational speed	Ω_{nom}	3000	rpm
Maximum rotational speed	Ω_{lim}	3600	rpm
Nominal power	P_{nom}	300	kW
Control parameter a	a_{ref}	0.015	$W\,s^b$
Control parameter b	b	3	–

Fig. 7. Power Spectral density of sea states s_3, s_4, s_6, and s_7.

a frequency step Δf. The wave signal $\zeta(x,t)$ is generated at position x in the wave flume as:

$$\zeta(x,t) = \sum_{j=0}^{N} \zeta_j \cos\left(kx - 2\pi f_j\, t + \phi_j\right), \tag{27}$$

where $\zeta_j = \sqrt{2\,S_\eta(f_j)\,\Delta f}$. The duration of each test was 20 min at prototype scale, as suggested in Ref. [42]. In the case of irregular waves, the entire time series was taken into account in the analysis, as reflections cannot be avoided. The sea states analysed in the study are summarised in Table 3, in which experimental characteristics are reported. Additionally, the power spectral density for s_3, s_4, s_6, and s_7 are presented in Fig. 7.

The accuracy of the irregular wave generation is verified by comparing different tests of the same wave in terms of the moments of the wave spectrum that define the significant wave height H_s and the peak frequency f_p. A constant peak enhancement factor appropriated for ocean waves is chosen equal to 3.3. It is important to ensure the repeatability of irregular waves for consistent evaluation of systems under varying wave conditions. The standard deviations of the peak frequency σ_{f_p} and the significant height σ_{H_s} are shown in Table 3 for sea states from s_1 to s_8, considering four repetitions each. There are no significant deviations from the statistical analysis, except for the significant height of sea state s_1 due to the limitations of the wavemaker in generating small waves.

Table 3 lists the peak frequencies and significant wave heights of the sea of spectra used in the current experiments.

4.3. Turbine diameter effect

To delve deep into the behaviour of the Wells turbine, it is possible to evaluate the effectiveness of the control action, considering that the turbine is controlled in real-time during the experiment, with the aim of tuning the best turbine size. Turbine diameter selection has a significant impact on PTO system dynamics, namely controllability and safe operation.

The control law given by Eq. (12) aims to operate the Wells turbine close to its optimum efficiency. However, it does not prevent compressible flow effects in the turbine rotor blades and does not guarantee that the mechanical stress limits for both the turbine blades and the electrical generator will not be exceeded due to centrifugal forces. These effects can be addressed indirectly by selecting an appropriate turbine rotor diameter, see [43] for further details. To avoid compressible flow effects in the Wells turbine rotor blades the maximum allowable blade tip speed is limited to $v_{tip,lim} = \Omega D/2 = 180\,m/s$ [22]. In the present work it has been assumed that the maximum allowable speed is limited by the electric generator. A typical off-the-shelf electric generator is assumed to be limited to $\Omega_{lim} = 3600$ rpm. The selection of the turbine rotor diameter is therefore limited by $v_{tip,lim}$ and Ω_{lim}.

Different sizes of Wells turbine have been analysed. For this type of device, subjected to regular and irregular waves, the Wells turbine operating within the safety stress limits is characterised by a nominal power P_{nom} of 300 kW and a minimum diameter of 1.35 m. The four different diameters analysed are summarised in Table 2, keeping the nominal power and the maximum rotational speed constant. The inertia I and the parameter a resulting from the control law have been scaled according to Froude's similarity, resulting

$$I = I_{ref} \left(\frac{D}{D_{ref}}\right)^5, \tag{28}$$

$$a = a_{ref} \left(\frac{D}{D_{ref}}\right)^5, \tag{29}$$

with respect to a known reference diameter [35]. A summary of the reference characteristics of the Wells turbine is given in Table 4.

4.4. Hydrodynamic behaviour

The hydrodynamic behaviour of the device is presented in this Section in terms of the response amplitude operator of the water column inside the air chamber [44],

$$RAO_z = \frac{A_z}{A_w}, \tag{30}$$

where A_z is the mean amplitude of OWC displacement and A_w is mean wave amplitude. The results from the regular wave tests are presented for ease of interpretation. The results are presented for the case of the for the Wells turbine and orifice plate simulating an impulse turbine. Fig. 8 shows the overlap of four area ratios S for the curves obtained by regular waves.

Both configurations exhibit a similar trend, with higher RAO values observed at frequencies between 0.5 and 0.7 Hz. However, comparing the RAOs obtained for the two turbines, the Wells turbine case shows a greater response than the impulse turbine case. In detail, for the Wells turbine, the device shows a greater response with an area ratio of 2%, peaking at frequencies between 0.67 and 0.7 Hz. For the other area ratios, the magnitude of the RAO is similar, but the peaks occur
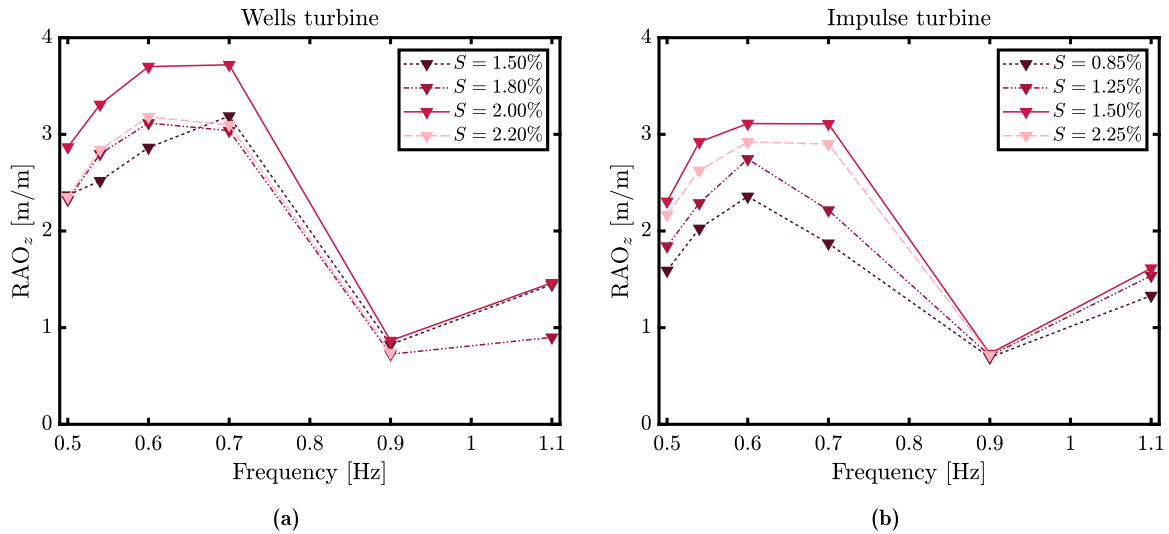
Fig. 8. Response amplitude operator of the OWC free surface with the WEC equipped with (a) Wells turbine and (b) impulse turbine for different area ratio S (turbines' size) in regular waves.

at different frequencies. Specifically, the RAO for the smallest area ratio of 1.5% peaks at 0.7 Hz, while those for area ratios of 1.8% and 2% peak at 0.67 Hz. This is because decreasing the turbine area, and thus increasing the pressure inside the chamber, results in a reduced variation in water level. Consequently, the damping obtained from the ratio between flow rate and pressure affects the hydrodynamics of the system, shifting the response peak to higher frequencies (thus corresponding to less energetic waves). In the case of the impulse turbine, the RAO curve with the highest magnitude is observed for an area ratio of 1.5%. Similarly to the Wells turbine case, the frequencies corresponding to higher RAO values are between 0.6 Hz and 0.7 Hz. All the curves show a peak at the frequency of 0.67 Hz. As the area ratio increases, the RAO also increases at frequencies towards 0.5 Hz, for the same reasons explained for the Wells turbine. This analysis is presented to provide the reader with an understanding of the device's behaviour from a hydrodynamic perspective. It is important to comprehend how the device responds when changing the type of turbine. On one hand, it is beneficial for the influence of the PTO on the device to be minimal so that the hydrodynamics can be studied independently and the design can be optimized. On the other hand, knowing which PTO allows the device to perform better paves the way for optimizing energy extraction by focusing on turbine control and improving predictability.

5. Results

Following a comprehensive analysis of the test conditions, including device operation, hydrodynamic response and the constraints of the flume environment and wave generation, this Section aims to demonstrate the effectiveness of the experimental representation of a Wells turbine using a real-time model.

5.1. Wells turbine experimental representation

From the real-time model, the controlled turbine flow rate and the diaphragm diameter are considered as outputs. To ensure that the Wells turbine is accurately represented, the air flow rate passing through the diaphragm, which accounts for the instantaneous damping effect on the hydrodynamic behaviour of the device, is compared with the flow rate of the controlled turbine and the turbine curve on which the real-time model is based to virtually represent the Wells turbine, shown in Fig. 3.

The volumetric flow rate Q_{OWC} is calculated from Eq. (1) as

$$Q_{OWC} = -A_{OWC} \frac{\rho_{in}}{\rho_c} \left(\frac{\Delta \dot{p}}{\gamma (\Delta p + p_{atm})} (h_0 - z) - \dot{z} \right), \tag{31}$$

where z is the OWC free surface position, h_0 is the height of the air chamber at initial conditions, A_{OWC} is the area of the air chamber.

Fig. 9(a) illustrates the dimensionless flow rate calculated as a function of: (i) the experimental Wells turbine flow rate curve $\Phi = f_\Phi(\Psi)$; (ii) the experimental Wells turbine flow rate curve $\Phi = f_\Phi(\Psi)$ where the pressure coefficient is calculated as $\Psi = \Delta p_{exp}/(\rho_{atm} \Omega_{num}^2 D^2)$ where Δp_{exp} is the experimental pressure head at the prototype scale; and (iii) the displacement of the OWC free surface over $\Omega_{num} D^3$ where Ω_{num} is the rotational speed as calculated in the HIL controller. The results are presented for the case of irregular wave $f_p = 0.67\,\text{Hz}$, $H_s = 0.0219\,\text{m}$ and an area ratio $S = 2\%$. It is shown that the experimental flow rate is congruent with turbine curve trend, that can be considered as nearly linear. The results plotted in Fig. 9(b) are depicted in terms of twice the standard deviation with respect the mean value of Φ calculated for Q_{OWC}. The standard deviation region shows that the accuracy decreases for the higher values of the pressure coefficient.

The comparison between the dimensionless turbine flow rate calculated using the imposed diameter by the controller D_{set} and the diameter obtained as measured by the encoder D_{fb} is shown in Fig. 10. In this way, the quality of the setup is checked, in particular the ability of the servomotor to effectively track the signal derived from the model. It can be seen that the flow rate from the feedback signal is not accurate around zero. However, this unwanted effect is not expected to influence the performance of the OWC power plant as the pneumatic power tends to zero.

To further validate the observed linear trend of the Wells turbine, the flow rate has been also evaluated for the impulse turbine, represented by a fixed orifice for area ratio S equal to 1.5%. It is important to note that the impulse turbine was not tested in real time, as it can be satisfactorily modelled by a fixed orifice, independent of the rotational speed. The dimensionless flow rate, evaluated using experimental pressure data and variations in the free surface area of the water within the air chamber, is shown in Fig. 11. These measurements were taken while maintaining a constant rotational speed, equivalent to the nominal speed of a reference impulse turbine [35]. The reference curve, presented in Fig. 3(b), illustrates that the trend of the results closely follows the reference curve, which tends towards a quadratic relationship (see Fig. 11).
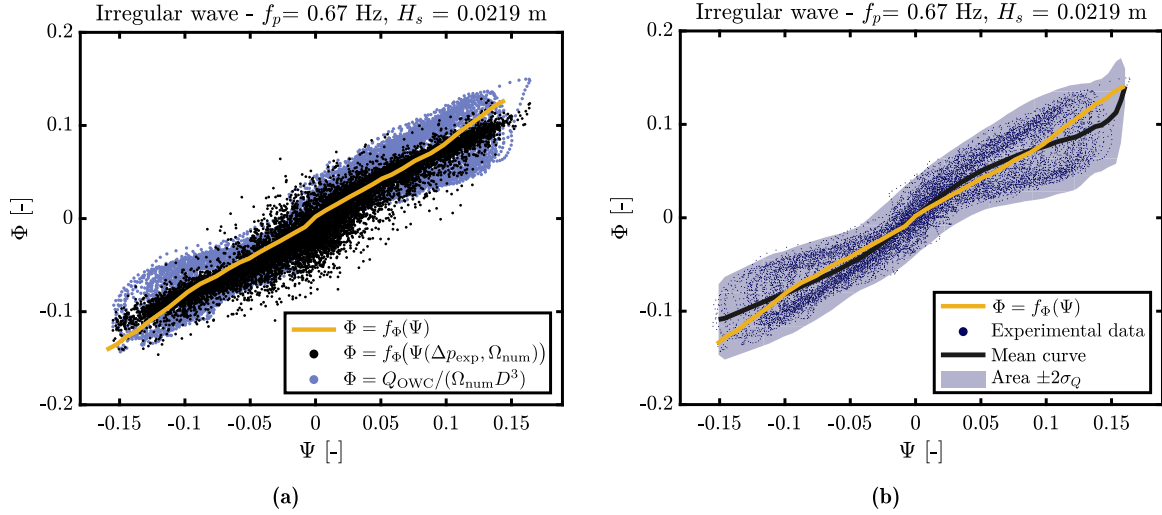
Fig. 9. (a) Comparison between the dimensionless flow rate of the Wells turbine shown in Fig. 3 with the experimental data, where the flow rate is estimated using Eq. (31) and the rotational speed is calculated from Eq. (9). (b) Mean value and standard deviations of the dimensionless flow rate inside the air chamber.
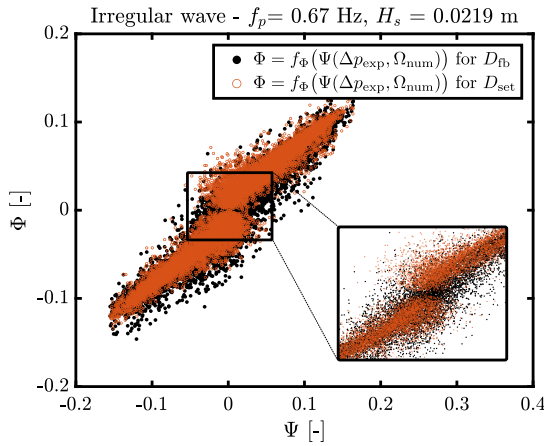

Fig. 10. Comparison between dimensionless turbine flow rate calculated using the output diameter D_{set} from the model and the feedback diameter D_{fb} from the encoder.

Fig. 11. Comparison between the dimensionless flow rate of the impulse turbine shown in Fig. 3(b) with the experimental data, where the flow rate is estimated using Eq. (31) and the rotational speed is calculated from Eq. (9).

5.2. Comparison of the pneumatic power available for Wells and impulse turbines

Wells turbine and impulse turbine are compared in this Section in terms of the mean pneumatic power available defined as

$$\bar{P}_{pneu} = \frac{1}{t_f - t_i} \int_{t_i}^{t_f} \Delta p \, Q \, dt, \tag{32}$$

where t_i and t_f are the initial and final integration time instants. The mean pneumatic power available for both turbines is presented in Fig. 12. The Fig. 12 shows that the two turbines have similar trend behaviour. The sea states are ordered in ascending frequency. In both cases studied, the pneumatic power is close to zero at lower frequencies and increases as the frequency rises. For the Wells turbine, two main trends are observed: one where the pneumatic power for the area ratio at 1.5% is generally higher than the others, except for the area ratio at 2%, which is higher for sea states from s_3 to s_1. In the case of the impulse turbine, the lower area ratio corresponds to greater pneumatic power for all sea states. Although it is expected greater pneumatic power extraction for more energetic waves (i.e., at lower frequencies),
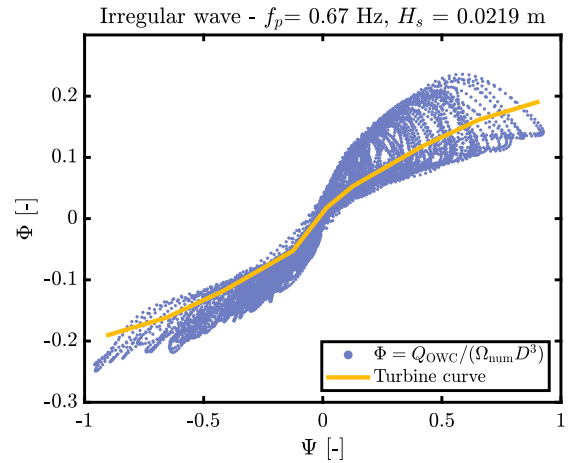
it is important to consider the phase shift between the pressure and the water level inside the chamber due to the compressibility of air. Specifically, constructive interactions in terms of extracted power occur as the phase shift between Δp and z decreases, which happens at lower frequency sea states. Conversely, as wave power increases, the phase shift also increases, leading to destructive interactions.

The pneumatic capture width (CW) evaluates the performance of both turbine types as a function of the sea state and area ratio S. The CW is defined as

$$CW = \frac{\bar{P}_{pneu}}{\bar{P}_{wave}}, \tag{33}$$

where $\bar{P}_{wave}$ is the wave power defined as the transport of wave energy E per unit wave crest length [39], as given by

$$E = \rho g m_0, \tag{34}$$

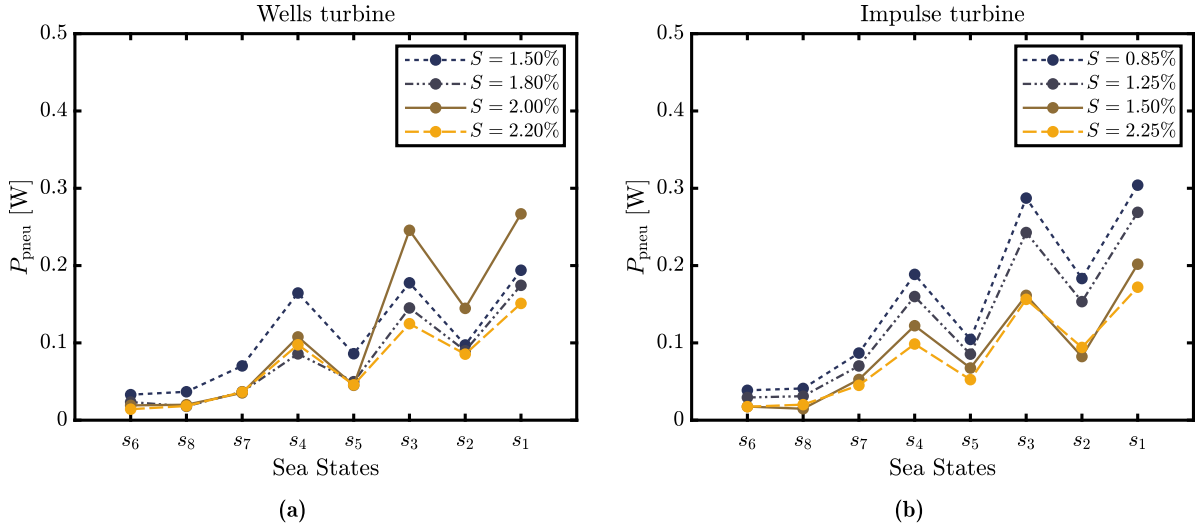$$\bar{P}_{wave} = E c_g, \tag{35}$$

Fig. 12. Mean available pneumatic power for (a) the Wells turbine simulator and (b) the impulse turbine simulator in sea states s_1 to s_8 for four area ratios. The sea states are ordered by increasing wave power.
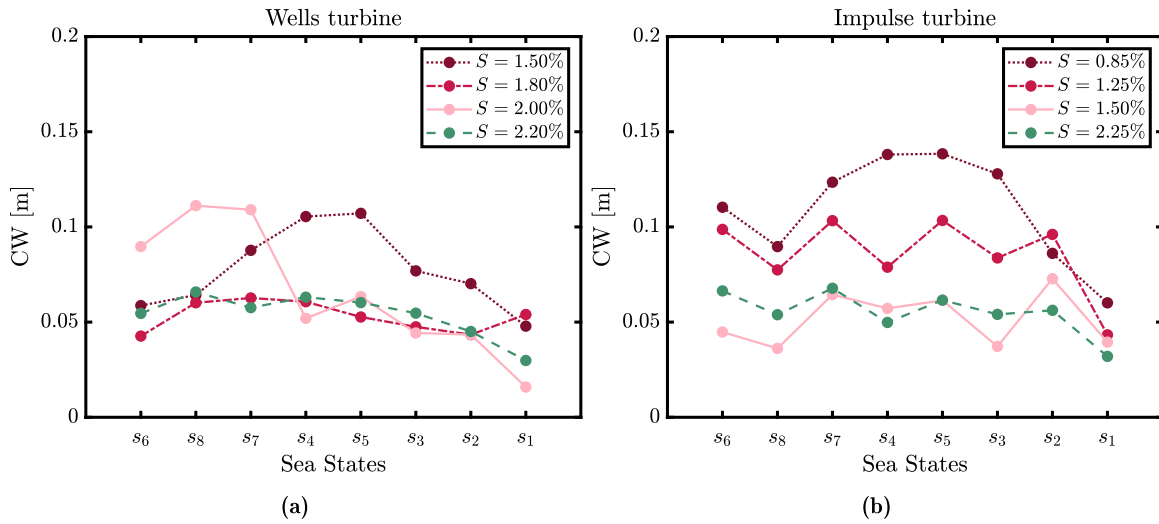

Fig. 13. (a) CW evaluated for Wells turbine simulator in sea states s_1 to s_8 for four area ratios. (b) CW evaluated for impulse turbine simulator in sea states s_1 to s_8 for four area ratios.

where m_0 is the zero-order moment and it represent the area under the wave spectral curve, defined as $m_0 = \sum_{i=0}^{N} a^2/2$ which is the total variance of the wave record obtained by the sum of the variances of the individual spectral components. Wave energy is calculated considering the deep water or shallow water formulation, depending on group velocity c_g of each the sea state.

For both types of turbines, the CW is higher for sea states s_4 and s_5, which are close to the resonance frequency of the OWC, in accordance with the hydrodynamic behaviour shown in Fig. 8. Fig. 13 shows that the area ratio S giving the highest CW is 1.5% for the Wells turbine case and 0.85% for the impulse turbine case, both for sea state s_4. More specifically, in the case of Wells turbines, the area ratio for $S = 2\%$ shows high values for sea states characterised by high frequencies, unlike the other cases. This suggests that the choice of turbine size should reflect a careful analysis of the wave resource, with the aim of matching the turbine diameter to the most frequent waves at the site. For the other value of S there are no relevant differences in CW and trend shape.

In the case of an impulse turbine, the CW decreases as the area ratio S increases. This result reveals that the best performance is obtained with smaller turbines compared to Wells turbines. Additional tests should be carried out for area ratios lower than $S = 0.85\%$.

To conclude the discussion on the performance in terms of CW, the results show that for the U-OWC power plant studied, it is advantageous to install an impulse turbine, as it generally has higher CW values, especially in the best case scenario. Furthermore, impulse turbines represent the best compromise, considering that the choice of the best turbine type should be based on a trade-off between efficiency and cost.

The Wells turbine has several aerodynamic and mechanical constraints that result from an mean rotational speed that is typically twice of the impulse turbine [43]. The main objective of the rotational speed control on the Wells turbines is to keep the turbine close to its optimum efficiency and to prevent aerodynamic stall, which occurs when the pressure coefficient exceeds a critical value, see Fig. 3. The need to avoid compressible flow effects in the Wells turbine rotor blades introduces a further aerodynamic constraint into the control strategy by limiting the maximum allowable blade tip speed of $v_{\text{tip,lim}} = 180$ m/s.
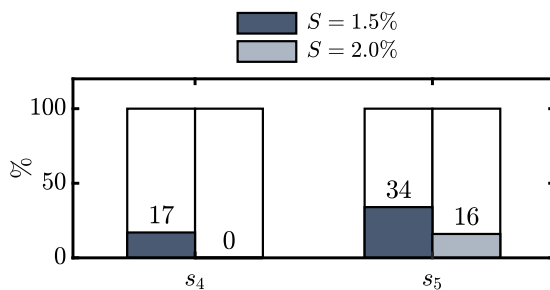
Fig. 14. Percentage of times the tip speed exceeds $v_{\text{tip, lim}}$, for area ratios $S = 1.5\%$ and $S = 2\%$.

Fig. 14 analyses the number of occurrences where the speed exceeded the limit $v_{\text{tip,lim}}$. The results are shown for the cases $S = 1.5\%$ and $S = 2\%$, which are characterised by the highest CWs. For both sea states, the percentage of times the limit is exceeded is lower for $S = 2\%$ than for $S = 1.5\%$. In both cases, the rotational speed of the turbine exceeds the indicated limit for at least one sea state. It can be concluded that, despite the higher power of the $S = 1.5\%$ case, the better choice for turbine size is $S = 2\%$. Further tests should be carried out in order to find the optimum diameter of the turbine to comply with the tip limit speed.

6. Conclusions

The paper presents a new methodology for simulating Wells turbines in small-scale experimental tests of oscillating-water-column (OWC) wave energy converters. The aim was to accurately reproduce the experimental flow rate curve of a given Wells turbine. This was done using a diaphragm whose diameter is adjusted in real-time based on the instantaneous relative pressure of the OWC chamber and the instantaneous rotational speed of the turbine. The rotational speed was calculated using a configuration where the dynamics of the turbine generator set is simulated at prototype scale in a hardware-in-the-loop configuration.

The methodology has been experimentally validated in a wave flume using a fixed U-shaped OWC. The system has been tested under regular and irregular wave loads. The wave generation analysis was presented to highlight the limitations of the wave flume and the experimental environment. The experimental results proved that the desired flow rate curve of the selected Wells turbine geometry could be imposed. This experimental representation of a Wells turbine can be seen as a replacement for the methods previously used, overcoming the impossibility of studying the full dynamics of the Wells turbine at model scale in a wave flume, including the rotation speed variation effect.

For the sake of comparison, an ideal impulse turbine was also simulated in the experimental setup. Several turbine diameters were examined. The comparison between the Wells turbine and the impulse turbine was made in terms of the capture width. Several turbine diameters have been considered and the value that gives the highest capture width has been found.

Further studies should focus on the performance investigation, increasing the number of tests to better understand the characteristics of the U-OWC power plant equipped with a Wells turbine. More attention should be dedicated to the set-up. The comparison between the output diameter and the feedback diameter shows no correspondence around zero, due to the chosen actuator mechanism.

CRediT authorship contribution statement

Beatrice Fenu: Writing – original draft, Validation, Software, Methodology, Investigation, Formal analysis, Conceptualization.

João C.C. Henriques: Writing – review & editing, Validation, Supervision, Software, Project administration, Methodology, Investigation, Conceptualization. **Mattia Glorioso:** Visualization, Software, Investigation. **Luís M.C. Gato:** Writing – review & editing, Validation, Funding acquisition, Conceptualization. **Mauro Bonfanti:** Writing – review & editing, Validation, Supervision, Software, Investigation, Funding acquisition.

Declaration of competing interest

The authors declare that they have no known competing financial interests or personal relationships that could have appeared to influence the work reported in this paper.

Data availability

Data will be made available on request.

References

[1] Lewis A, Huckerby SEJ, Lee KS, Musial W, Pontes T, Torres-Martinez J, et al. Ocean energy. In: Edenhofer O, Pichs-Madruga R, Sokona Y, Seyboth K, Matschoss P, Kadner S, Zwickel T, Eickemeier P, Hansen G, Schlömer S, von Stechow C, editors. IPCC special report on renewable energy sources and climate change mitigation. Cambridge University Press; 2012, p. 497–534, https://www.ipcc-wg3.de/report/IPCC_SRREN_Full_Report.pdf. [Accessed 25 March 2024].

[2] Wave Energy Scotland (WES). Ocean energy europe. 2015, https://www.oceanenergy-europe.eu/ocean-energy/wave-energy/. [Accessed 25 March 2024].

[3] Guo B, Ringwood JV. A review of wave energy technology from a research and commercial perspective. IET Renew Power Gener 2021;15:3065–90. http://dx.doi.org/10.1049/rpg2.12302.

[4] Ahamed R, McKee K, Howard I. Advancements of wave energy converters based on Power Take Off (PTO) systems: A review. Ocean Eng 2020;204:107248. http://dx.doi.org/10.1016/j.oceaneng.2020.107248.

[5] Clemente D, Rosa-Santos P, Taveira-Pinto F. On the potential synergies and applications of wave energy converters: A review. Renew Sustain Energy Rev 2021;135:110162. http://dx.doi.org/10.1016/j.rser.2020.110162.

[6] Heath TV. A review of oscillating water columns. Phil Trans R Soc A 2012;370:235–45. http://dx.doi.org/10.1098/rsta.2011.0164.

[7] Falcão AFO, Henriques JCC. Oscillating-water-column wave energy converters and air turbines: A review. Renew Energy 2016;85:1391–424. http://dx.doi.org/10.1016/j.renene.2015.07.086.

[8] Andres AD, Medina-Lopez E, Crooks D, Roberts O, Jeffrey H. On the reversed LCOE calculation: Design constraints for wave energy commercialization. Int J Mar Energy 2017;18:88–108. http://dx.doi.org/10.1016/j.ijome.2017.03.008.

[9] Bailey H, Robertson BRD, Buckham BJ. Wave-to-wire simulation of a floating oscillating water column wave energy converter. Ocean Eng 2016;125:248–60. http://dx.doi.org/10.1016/j.oceaneng.2016.08.017.

[10] Sheng W. Motion and performance of BBDB OWC wave energy converters: I, hydrodynamics. Renew Energy 2019;138:106–20. http://dx.doi.org/10.1016/j.renene.2019.01.016.

[11] Howe D, Nader J-R, Macfarlane G. Experimental investigation of multiple oscillating water column wave energy converters integrated in a floating breakwater: Energy extraction performance. Appl Ocean Res 2020;97. http://dx.doi.org/10.1016/j.apor.2020.102086.

[12] Elhanafi A, Macfarlane G, Fleming A, Leong Z. Experimental and numerical investigations on the hydrodynamic performance of a floating–moored Oscillating Water Column wave energy converter. Appl Energy 2017;205:369–90. http://dx.doi.org/10.1016/j.apenergy.2017.07.138.

[13] Kelly T, Dooley T, Campbell J, Ringwood JV. Comparison of the experimental and numerical results of modelling a 32-Oscillating Water Column (OWC), V-shaped floating wave energy converter. Energies 2013;6:4045–77. http://dx.doi.org/10.3390/en6084045.

[14] Pérez-Collazo C, Greaves D, Iglesias G. A review of combined wave and offshore wind energy. Renew Sustain Energy Rev 2015;42:141–53. http://dx.doi.org/10.1016/j.rser.2014.09.032.

[15] He F, Leng J, Zhao X. An experimental investigation into the wave power extraction of a floating box-type breakwater with dual pneumatic chambers. Appl Ocean Res 2017;67:21–30. http://dx.doi.org/10.1016/j.apor.2017.06.009.

[16] Torre-Enciso Y, Ortubia I, Aguileta LI, Marqués J. Mutriku wave power plant: From the thinking out to the reality. In: Proc. of the 8th European wave and tidal energy conference. 2009, p. 319–29.

[17] Boccotti P. On a new wave energy absorber. Ocean Eng 2003;30:1191–200. http://dx.doi.org/10.1016/S0029-8018(02)00102-6.

[18] Arena F, Romolo A, Malara G, Fiamma V, Laface V. The first full operative U-OWC plants in the port of Civitavecchia. In: ASME 2017 36th international conference on ocean, offshore and arctic engineering. 2017, http://dx.doi.org/10.1115/OMAE2017-62036, V010T09A022.

[19] Malara G, Arena F. Response of U-oscillating water column arrays: Semi-analytical approach and numerical results. Renew Energy 2019;138:1152–65. http://dx.doi.org/10.1016/j.renene.2019.02.018.

[20] Shehata AS, Xiao Q, Saqr KM, Alexander D. Wells turbine for wave energy conversion: A review. Int J Energy Res 2017;41:6–38. http://dx.doi.org/10.1002/er.3583.

[21] Suzuki M, Takao M, Satoh E, Nagata S, Toyota K, Setoguchi T. Performance prediction of OWC type small size wave power device with impulse turbine. J Fluid Sci Technol 2008;3:466–75. http://dx.doi.org/10.1299/jfst.3.466.

[22] Rosati M, Henriques JCC, Ringwood JV. Oscillating-water-column wave energy converters: A critical review of numerical modelling and control. Energy Convers Manag: X 2022;16:100322. http://dx.doi.org/10.1016/j.ecmx.2022.100322.

[23] Orphin J, Schmitt P, Nader J-R, Penesis I. Experimental investigation into laboratory effects of an OWC wave energy converter. Renew Energy 2022;186:250–63. http://dx.doi.org/10.1016/j.renene.2021.12.092.

[24] Gonçalves RAAC, Teixeira PRF, Didier R, Torres FR. Numerical analysis of the influence of air compressibility effects on an oscillating water column wave energy converter chamber. Renew Energy 2020;153:1183–93. http://dx.doi.org/10.1016/j.renene.2020.02.080.

[25] Dimakopoulos AS, Cooker MJ, Bruce T. The influence of scale on the air flow and pressure in the modelling of oscillating water column wave energy converters. Int J Mar Energy 2017;19:272–91. http://dx.doi.org/10.1016/j.ijome.2017.08.004.

[26] Cheng Y, Fu L, Dai S, Collu M, Ji C, Yuan Z, et al. Experimental and numerical investigation of WEC-type floating breakwaters: A single-pontoon oscillating buoy and a dual-pontoon oscillating water column. Coast Eng 2022;177:104188. http://dx.doi.org/10.1016/j.coastaleng.2022.104188.

[27] Cheng Y, Fu L, Dai S, Collu M, Cui L, Yuan Z, et al. Experimental and numerical analysis of a hybrid WEC-breakwater system combining an oscillating water column and an oscillating buoy. Renew Sustain Energy Rev 2022;169:112909. http://dx.doi.org/10.1016/j.rser.2022.112909.

[28] Liu Z, Xu C, Kim K, Zhang X, Ning D. Hydrodynamic and energy-harvesting performance of an isolated oscillating water column device: An experimental study. Coast Eng 2024;189:104459. http://dx.doi.org/10.1016/j.coastaleng.2024.104459.

[29] Joensen B, Bingham HB, Read RW, Nielsen K, Trevino JB. Hydrodynamic analysis of one-way energy capture by an oscillating water column wave energy device. Energy Rep 2023;9:5306–22. http://dx.doi.org/10.1016/j.egyr.2023.04.052.

[30] Stefanizzi M, Camporeale SM, Torresi M. Experimental investigation of a Wells turbine under dynamic stall conditions for wave energy conversion. Renew Energy 2023;214:369–82. http://dx.doi.org/10.1016/j.renene.2023.05.120.

[31] Gaspar JF, Pinheiro RF, Mendes MJGC, Kamarlouei M, Guedes Soares C. Review on hardware-in-the-loop simulation of wave energy converters and power take-offs. Renew Sustain Energy Rev 2024;191:114144. http://dx.doi.org/10.1016/j.rser.2023.114144.

[32] Fox BN, Gomes RPF, Gato LMC. Analysis of oscillating-water-column wave energy converter configurations for integration into Caisson breakwaters. Appl Energy 2021;295:117023. http://dx.doi.org/10.1016/j.apenergy.2021.117023.

[33] Falcão AFO, Henriques JCC. The spring-like air compressibility effect in oscillating-water-column wave energy converters: Review and analyses. Renew Sustain Energy Rev 2019;112:483–98. http://dx.doi.org/10.1016/j.rser.2019.04.040.

[34] Tease WK, Lees J, Hall A. Advances in oscillating water column air turbine development. In: Proc. 7th European wave and tidal energy conference. 2007.

[35] Henriques JCC, Portillo JCC, Sheng W, Gato LMC, Falcão AFO. Dynamics and control of air turbines in oscillating-water-column wave energy converters: Analyses and case study. Renew Sustain Energy Rev 2019;112:571–89. http://dx.doi.org/10.1016/j.rser.2019.05.010.

[36] Falcão AFO, Henriques JCC. Model-prototype similarity of oscillating-water-column wave energy converters. Int J Mar Energy 2014;6:18–34. http://dx.doi.org/10.1016/j.ijome.2014.05.002.

[37] Munson BR, Rothmayer AP, Okiishi TH. Fundamentals of fluid mechanics. 7th ed. Wiley; 2012.

[38] Hughes SA. Physical models and laboratory techniques in coastal engineering. Advanced series on ocean engineering, World Scientific; 1993.

[39] World Meteorological Organization. Guide to wave analysis and forecasting. WMO (series), Secretariat of the World Meteorological Organization; 1998.

[40] Hasselmann K, Barnett TP, Bouws E, Carlson H, Cartwright DE, Eake K, et al. Measurements of wind-wave growth and swell decay during the joint North Sea wave project (JONSWAP). Deut Hydrogr Z 1973;8:1–95.

[41] Mérigaud A, Ringwood JV. Free-surface time-series generation for wave energy applications. IEEE J Ocean Eng 2018;43:19–35. http://dx.doi.org/10.1109/JOE.2017.2691199.

[42] ITTC. Recommended procedures and guidelines: Wave energy converter model test experiments. 2021, https://www.ittc.info/media/9745/75-02-07-037.pdf.

[43] Falcão AFO, Henriques JCC, Gato LMC. Self-rectifying air turbines for wave energy conversion: A comparative analysis. Renew Sustain Energy Rev 2018;91:1231–41. http://dx.doi.org/10.1016/j.rser.2018.04.019.

[44] Perez T. Ship motion control: course keeping and roll stabilisation using rudder and fins. Advances in industrial control, London: Springer; 2006.